# Quantum holography enhanced by object-uncorrelated photons

Yiqian Yang,[1,*] Zhixiang Li,[2,4,*] Zhengzhong Huang,[1] Andrew Forbes,[3,†] Liangcai Cao,[1,‡] Keyu Xia,[2,4,5,§] and Yanqing Lu[2,4,5,‖]

[1] *Department of Precision Instruments, Tsinghua University, 100084 Beijing, China*
[2] *College of Engineering and Applied Sciences, Nanjing University, Nanjing, 210023 Jiangsu, China*
[3] *School of Physics, University of Witwatersrand, Johannesburg, 2000, South Africa*
[4] *National Laboratory of Solid State Microstructures, Nanjing University, Nanjing, 210093 Jiangsu, China*
[5] *Hefei National Laboratory, Hefei, 230088 Anhui, China*

(Received 15 April 2025; accepted 10 November 2025; published 31 December 2025)

Quantum holography exploits quantum correlation in entangled photon pairs to enhance holography. An inherent principle of holography is that each partial hologram can enhance the reconstruction of the entire object, a property that has not yet been explored in the quantum realm. The current fabrication technology for single-photon detectors is limited, making it extremely challenging to manufacture large-area detectors. Since resolution is directly related to the system aperture, achieving a resolution equivalent to that of a large-area detector under the constraint of a limited detection area is a key challenge for realizing high-resolution quantum holography. Here we demonstrate that the spatial correlations of entangled photons can extract crucial additional information from photon wave packets beyond the boundaries of the experimentally recorded region, where the photons have no direct interaction with the object. We validate the approach experimentally and benchmark it against the approach using only the detection area, achieving the advancements with an increase of up to 15 dB in signal-to-noise ratio and up to approximately tenfold improvement in structural similarity. We show the versatility of the approach by demonstrating significantly improved performance across various objects, including quantum holography of complex biological specimens. This work can advance the nascent field of quantum holography and accelerate its application in life sciences and biological systems.

DOI: 10.1103/b2hb-7zj5

## I. INTRODUCTION

Holography, a cornerstone in optical imaging, traditionally harnesses the classical interference of light waves for both amplitude and phase reconstruction [1,2]. This versatile technique finds applications in various fields such as imaging [3–5], display [6,7], biological microscopy [8,9], lithography [10,11], optical neural networks [12–14], and optical security [15,16]. Conventionally, holography is realized by splitting a light beam into two parts and then combining them, where one beam illuminates the object to generate a scattering field and the other serves as a reference. The hologram can be produced by recording the interference of scattered and reference fields or through computational diffraction [17]. Nevertheless, the recombination of the split beams limits holography to a local technique, constraining its applicability in certain scenarios [18,19].

The quantum nature of light has inspired a variety of imaging modalities that use entanglement or correlations [20–22]. Quantum holography leverages the nonclassical properties of light and its interaction with the environment to overcome the limitations of classical holography [23–26]. Unlike quantum imaging, which typically focuses on capturing intensity or position information using entanglement or correlations, quantum holography aims to reconstruct both the amplitude and the phase of the optical field, enabling full-field imaging. In quantum holography, one mode of the entangled photon pair, typically generated via spontaneous parametric down-conversion (SPDC), serves as a reference, while the other mode is sent to probe the object [27–29]. The spatial and temporal correlations of photons can be utilized to extract the image and

*These authors contributed equally to this work.
†Contact author: andrew.forbes@wits.ac.za
‡Contact author: clc@tsinghua.edu.cn
§Contact author: keyu.xia@nju.edu.cn
‖Contact author: yqlu@nju.edu.cn

distance of the object on the basis of coincidence counting. In these entangled-photon-based or correlation-based methods, the coincidence between the photons significantly increases the signal-to-noise ratio (SNR) in noisy and lossy environments [30–33], increasing resolution [34, 35] and increasing interferometry stability [36]. Recently, an experiment using entangled photon pairs to obtain the cosine values of the phase of an unknown photon state was introduced [37]. This approach successfully achieved complete phase retrieval by using a suitable iterative algorithm and requires high-precision phase shift. Then, a quantum holography approach using the first-order incoherent beam to increase spatial resolution compared with classical coherent holography by a four-step phase shift was proposed [38]. In this method, holographic information is encoded in the second-order coherence of entangled light states, as phase cannot be extracted from classical interference measurements. This method needs the object to be polarization sensitive. Several other advances have been made in recent years, such as the use of nondegenerate quantum holography to convert imperceptible wavelengths into visible ones [39,40], and integration of quantum technology into wide-field transmission microscope setups to enable full-field phase retrieval with increased stability and resilience to stray light [41]. Moreover, combining quantum holography techniques with metasurfaces [42, 43], machine intelligence [44,45], adaptive optics [46–48], orbital angular momentum [49–51], and microscopy [52–54] opens a path for quantum holography to revolutionize various fields, offering unprecedented capabilities in imaging, sensing, communication, and data processing.

The current fabrication technology for single-photon detectors is limited, making it extremely challenging to manufacture large-area detectors. Since the resolution is directly related to the system aperture, achieving a resolution equivalent to that of a large-area detector under the constraint of a limited detection area is a key challenge for realizing high-resolution quantum holography. In holography, as extolled by Gabor [55], each partial hologram can add more information and thus improve the reconstruction of the entire object [56,57]. Such an important property has not yet been explored in quantum holography. Previous quantum holography encoded object information into a superposition [32] or entangled degree of freedom [38], but wasted high-frequency information hidden in wave packets outside the detection region, which can be extracted with the help of spatial correlations in quantum holography. It is important to harness such high-frequency information from a "virtual" hologram beyond the detection region. In this work, we achieve high-resolution and high-SNR quantum holography based on the combination of the advantages of quantum correlation and a holographic algorithm. We realize imaging equivalent to that of a large-area detector under a constrained quantum detector, where we add an aperture before the detector to simulate the limited detection region to prove our theory. We demonstrate that high-frequency information from the outer region can be extracted computationally to increase the resolution and SNR by using photon pairs that are not correlated with the object, i.e., those falling outside the usual recorded object-correlated spatial region. Building upon this principle, we demonstrate a quantum holography approach by fully utilizing all photon pairs to construct an extrapolated hologram, followed by applying an iterative reconstruction algorithm that integrates computer intelligence with quantum light [58]. We benchmark our approach, dubbed "the object-and-SPDC method," which uses both object-correlated photons and extrapolated object-uncorrelated photons, against previous quantum holography methods that rely solely on object-correlated photons, referred to as the "object-only method." Our approach demonstrates superior performance in reconstructing phase and amplitude objects and marks, to our knowledge, the first application of quantum holography for probing complex biological samples. Note that quantum imaging of biological samples was achieved very recently [46,59]. Our approach overcomes the limitations of resolution in previous quantum holography and solves specific object requirements. The comparisons reveal that the object-and-SPDC method achieves an averaged increase of up to 15 dB in the peak signal-to-noise ratio (PSNR) and up to tenfold in the structural similarity index measure (SSIM) compared with the object-only method. Besides, our diffraction-based holographic recording approach, rather than an interference-based approach, provides a pathway for enabling lensless quantum holography. These improvements imply significant advancement of quantum holography in biological microscopy and quantum encoding.

## II. CONCEPT AND PRINCIPLE

The concept and detailed experimental operation of our extrapolated quantum holography enabled by object-uncorrelated photons is schematically illustrated in Fig. 1. The first recording, similarly to previous quantum holography, captures photons that interact directly with the object within a limited detection area (namely, the object-correlated photons). In previous quantum holography, this detection area was constrained by the detector size. Here we simulate this limitation using a reduced aperture to validate our theory. Then the second recording, essentially a preliminary operation, captures the SPDC photon distribution when the object is removed. This records an extrapolated area containing photons that do not directly interact with the object (namely, the object-uncorrelated photons). The aperture is fully opened to capture the object-uncorrelated photons for construction of an extrapolated hologram, allowing additional information to be retrieved beyond the initially recorded region. Notably, this

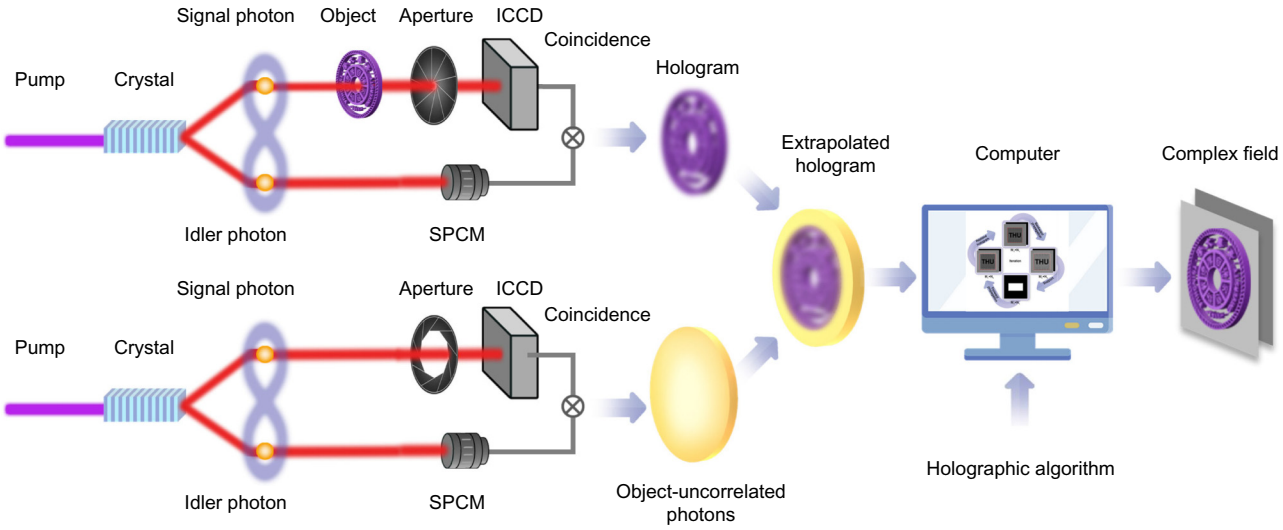


FIG. 1. Concept of extrapolated quantum holography. The photon pairs are generated by SPDC, with one interacting with the object. We first capture object-correlated photons and then capture object-uncorrelated photons when the object is removed. The object-uncorrelated photons are used to create an extrapolated hologram, extending beyond the boundaries of the initially record region. By use of Gabor's principle of holography, which differs from imaging, the information outside the object region is used to increase the spatial resolution and SNR of the object since it contains useful high-frequency information about the object. This is processed by a holographic algorithm to reconstruct a high-resolution complex field of the object, enabling detailed imaging with unprecedented clarity and precision. Shown here for the Tsinghua University logo.

is a single-frame method, meaning only the first recording is required experimentally. The SPDC photon distribution can be accurately calculated on the basis of the well-characterized properties of the nonlinear crystal [60]. Since the SPDC photon distribution is a standard aspect of most imaging system setups, in practice, a hologram can be captured with the use of the full detection region of the camera, and the outer SPDC photon distribution can be computed.

Incorporation of Gabor's principle of holography, which differs from direct imaging, allows information from the extrapolated region to increase the spatial resolution of the reconstruction. This enhancement arises from the inclusion of high-frequency components beyond the detected object-correlated region, which are critical for finer reconstruction details. The improvement is achieved by processing of the experimental data computationally with an extrapolation method, followed by use of an iterative reconstruction algorithm, as described in Appendix A. This extrapolated quantum holography approach leads to significant improvements with unprecedented clarity and precision. Furthermore, traditional holography typically records object information based on interference effects with the use of a $4f$ imaging system. In contrast, our method relies on diffraction to capture the intensity distribution of the object's diffracted field and reconstructs the corresponding phase from this intensity distribution. The key advantage of a noninterference structure is its ability to simplify the optical system, enabling lensless imaging. This shifts the imaging burden from the optical path to computational processing, where diffraction patterns captured by the detector are used to reconstruct the original light field distribution, ultimately achieving the imaging goal.

We now explain the concept rigorously, with full details in Supplemental Material (see "Art presentation of the concept" in Supplemental Material [61]). In heralded single-photon quantum holography, the imaging $k$ space can be decomposed through orthogonal mode decomposition. Each basis $|r\rangle$ is derived by computation of the outer products of column vectors from the Hadamard transform matrix, expressed as $|r\rangle_k = |r\rangle_{(x,y)} = H_x \otimes H_y$, where $\otimes$ represents the tensor product of two quantum states. By projection of the object onto the discrete transverse wave vector basis, each orthogonal mode captures distinct features of the object being imaged, and the object can be expressed as

$$|\psi_O\rangle = \sum_{j=1}^{n} \frac{1}{n} \sqrt{p_j} \exp(i\alpha_j) \, |r_O\rangle_j \,, \tag{1}$$

where $|\psi_O\rangle$ represents the state of the object. $p_j$ represents the statistical average of the object projected onto the basis wave vector $|r\rangle_j$, calculated through inner products $p_j = |\langle r_j | \psi_O \rangle|^2$, with $\alpha_j$ denoting the corresponding phase. Both the amplitude and the phase of the modes have been normalized. $n$ denotes the total number of discrete transverse wave vector basis states $|r\rangle_j$ in the $x$ and $y$ components. The limited size of the hologram imposes a constraint on the achievable SNR and resolution of the reconstruction. The distribution of a single photon is inherently

random. However, statistically, single photons illuminate the object uniformly, generating a continuous diffraction pattern beyond the recorded region. This extended pattern can be used to overcome the SNR and resolution limitations of the reconstruction. The statistical distribution of the idler photons from SPDC is expressed as

$$|\psi_I\rangle = \sum_{k=1}^{n} \frac{1}{n} |r_I\rangle_k , \tag{2}$$

as derived in Appendix C, where $|\psi_I\rangle$ represents the state of the idler photons. By extrapolation of the limited hologram of the object region with the extended photon distribution, the extrapolated hologram is obtained as

$$|\psi_H\rangle = |\psi_O\rangle \otimes |\psi_I\rangle = \sum_{j,k=1}^{n} \frac{1}{n^2} \sqrt{p_j} \exp(i\alpha_j) |r_O\rangle_j \otimes |r_I\rangle_k , \tag{3}$$

where $\psi_H$ represents the state of the hologram. The dimension of the matrix extends from $j$ to $j \times k$, allowing a comprehensive analysis of the quantum state, incorporating additional degrees of freedom or parameters. Although the extended part does not contain photons that interact with the object, it introduces more features and variations beyond the captured region, resulting in a more detailed and accurate analysis of the object. The increased SNR and resolution stem from better fitting of the series of wavelets constituting the wave front in the hologram plane when a larger area is available. By extrapolation of the hologram and the conducting of iterations, the dimensions of the quantum holography channel are extended, enabling access to previously unrecorded outer sections of the hologram. The emergence of extrapolated higher-order fringes in the hologram contributes to enhanced properties in object reconstruction. In essence, the use of object and SPDC photon information (object-and-SPDC method) is predicted to be superior to the use of algorithms that use only object information (object-only method). We test the algorithm numerically under a range of object and detector sizes (see "Minimum hologram region requirement" in Supplemental Material [61]), and external conditions such as loss and noise (see "Noise robustness" in Supplemental Material [61]). All results collectively underscore the superiority of our approach in quantum holography, showcasing its resilience to noise and its ability to produce high-quality reconstructions with limited initially captured data. Such findings hold promising implications for practical applications of quantum holography. Next, we test the concept and its numerical predictions experimentally with a range of object types.

## III. EXPERIMENTAL VALIDATION

To differentiate our approach from single-photon imaging, we require the experiment to herald a single photon that interacts with the object and that is recorded on a spatially resolved detector placed some distance away. The experimental setup of our extrapolated quantum holography is depicted in Fig. 2(a), with detailed information provided in Appendix B. Entangled signal-idler photon pairs at a wavelength of 810 nm are generated through SPDC by the pumping of a periodically poled potassium titanyl phosphate (PPKTP) nonlinear crystal at a wavelength of 405 nm, which is placed inside a Sagnac interferometer [62–64]. The idler photon is used to herald the signal photon illuminating the object and is then detected by an intensified charge-coupled device (ICCD; the detector). A delay line in the signal-mode path is used to compensate for the electronic delay and to ensure synchronicity of the entangled photons. The ICCD is placed at a distance of 1 mm to enable sufficient free-space diffraction of the object photons, which is essential for the reconstruction process. This distance allows the system to capture the first three orders of diffraction fringes. As illustrated in Figs. 2(b) and 2(c), we first capture the object-correlated (object-only) photons within a limited imaging area. We then calculate the distribution of SPDC photons when the object is removed (SPDC photons only). These photons are used to create an extrapolated hologram (object-and-SPDC method). Then the extrapolated hologram is iteratively calculated to reconstruct the amplitude and phase of the object. Two recordings are experimentally recorded for each object under identical conditions to obtain an extrapolated hologram to prove our concept here. However, in practice, only the first recording is experimentally needed. Replacement of the second recording with a calculated SPDC photon distribution makes no difference to the reconstruction results (see "SPDC photon distribution validation" in Supplemental Material [61]). This single-frame approach can reduce the acquisition time for both amplitude and phase reconstruction compared with the conventional four-step phase-shifting method. Besides, filling the extrapolated region with the SPDC photon distribution instead of random pixel values or flat pixel values ensures that, during the iterative reconstruction algorithm, the initial wave packet accelerates convergence and prevents the solution from settling into local minima rather than the global minimum (see "Extrapolation validation" in Supplemental Material [61]). The extrapolated hologram contains information approximately equivalent to the fifth-order diffraction fringes. While inclusion of even higher-order diffraction fringes could theoretically improve reconstruction quality, their contribution becomes negligible beyond the fifth order. This is because the first five diffraction orders already carry about 95% of the total optical energy. As a result, further extension offers limited

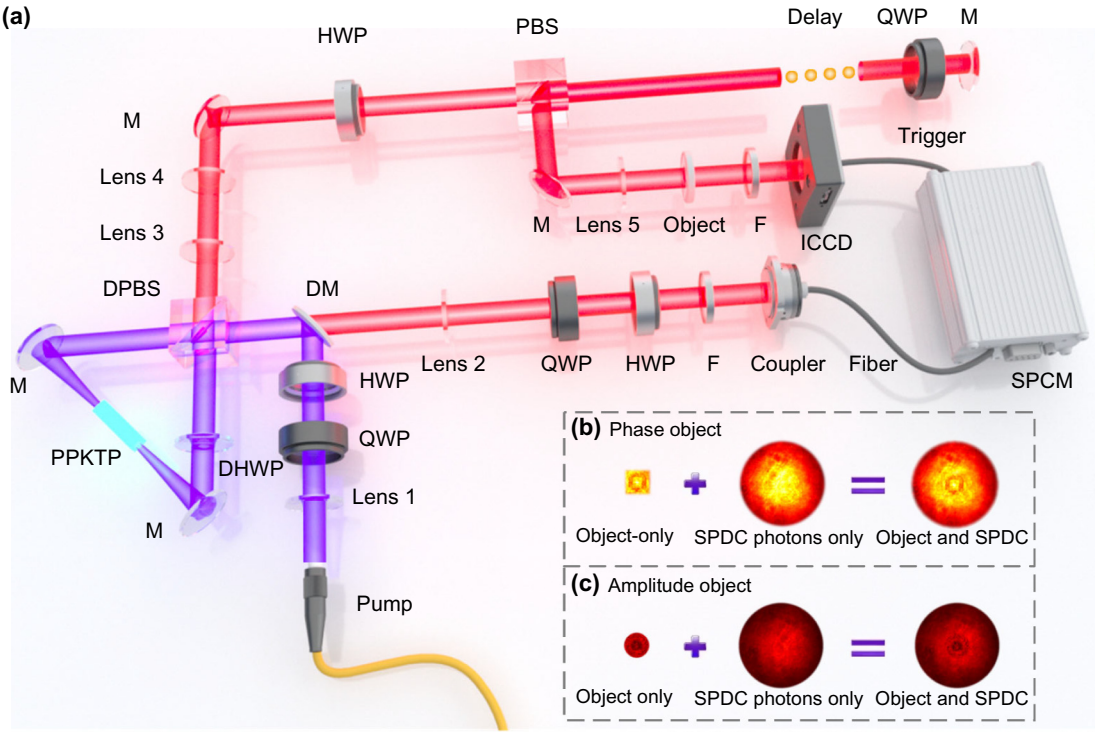


FIG. 2. Experimental setup and hologram extrapolation for quantum holography. (a) Experimental setup. Pump, $\lambda = 405$ nm; lens 1, focal length 200 mm; lenses 2–5, focal length 300 mm. For (b) the phase-only sample and (c) the amplitude-only sample, we capture the object-correlated photons (object only) within a limited area, and then extrapolate the SPDC photon distribution when the object is removed (SPDC photons only). Information from both images is used to form an extrapolated hologram (object and-SPDC) for calculation. The phase-only object consists of transparent squares with a length of 200 μm, each assigned a phase value of 1.2 rad. The amplitude-only object is a dot with a diameter of 100 μm. DHWP, dual-wavelength half-wave plate; DM, dual-wavelength mirror; DPBS, dual-wavelength polarizing beam splitter; F, filter: HWP, half-wave plate; QWP, quarter-wave plate; M, mirror; PBS, polarizing beam splitter.

benefits, while significantly increasing the computational cost and susceptibility to noise.

To demonstrate the effectiveness of the method, we initially test it using homemade objects well-characterized in the form of phase-only and amplitude-only samples. For comparison, the results from both the previous reconstruction approach (object-only method) and our method (object-and-SPDC method) are presented. The phase object, shown in Fig. 3(a), consists of two transparent squares, each with a side length of 200 μm and assigned a phase value of 1.2 rad. The detected object-only hologram, measuring $800 \times 600$ μm$^2$, is shown in Fig. 3(b), and the corresponding reconstruction results are shown in Fig. 3(c). The object-only approach fails to accurately capture the expected phase value, making it difficult to distinguish the features of the squares. The height profiles reveal the three-dimensional phase fluctuations, indicating that the object is largely submerged within the background. By combining the object-only hologram with the SPDC information, we form the extrapolated hologram with a size of $900 \times 700$ μm$^2$ for object reconstruction, with the results shown in Fig. 3(d). The object-and-SPDC approach accurately reflects the expected phase value of 1.2 rad, as indicated by the consistent yellow regions in the reconstruction. The height profiles of the three-dimensional phase fluctuations show that the object-and-SPDC approach clearly delineates the locations of the squares and provides more accurate phase values compared with the object-only method. To quantify the phase values experimentally, we examine the cross sections of the reconstructions in Fig. 3(e). The blue line, representing the object-and-SPDC method, demonstrates a phase difference of 1.2 rad from peak to valley and a width of around 200 μm, closely aligning with the green line, which represents the ground truth. In contrast, the red line, representing the object-only method, remains nearly constant around the baseline phase of 0.5, failing to recover the object's morphology. The PSNR and SSIM are used to quantify the performance of the two methods. The PSNR of the object-and-SPDC approach for two squares is 25.58 and 27.28 dB, respectively, while for the object-only approach it is 11.13 and 11.60 dB, respectively. The SSIM for the object-and-SPDC approach for two squares is 0.84 and 0.87, respectively, while for the object-only

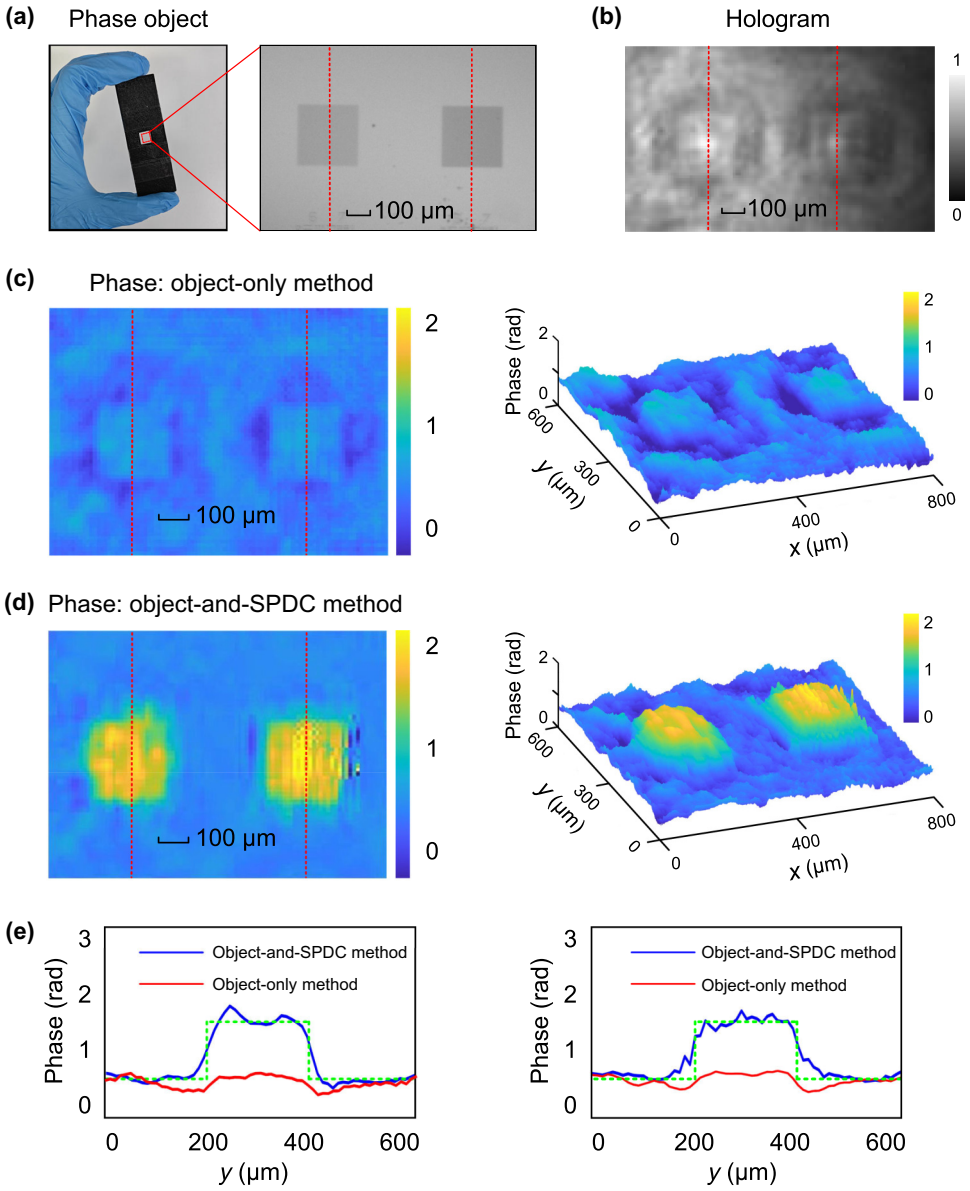


FIG. 3. Phase reconstruction. (a) Morphology of the phase object, consisting of transparent squares, each 200 μm in size and assigned a phase value of 1.2 rad. (b) Experimentally measured hologram of the phase object. (c) Phase reconstruction results obtained with the previous quantum holography approach (object-only method). The object-only approach struggles to distinguish the features of the squares, with the height profiles indicating that the object is largely submerged within the background. (d) Phase reconstruction results obtained with the proposed method (object-and-SPDC method). The object-and-SPDC approach accurately reflects the expected phase value of 1.2 rad, as indicated by the consistent yellow regions. The height profiles clearly delineate the locations of the squares and provide accurate phase values. (e) Cross sections of the reconstructions. The blue line, representing the object-and-SPDC method, displays a phase difference of 1.2 rad from peak to valley and a width of approximately 200 μm, closely matching the green line, which represents the ground truth. In contrast, the red line for the object-only method remains nearly constant at a baseline phase of 0.5, failing to accurately recover the object's morphology.

approach it is 0.07 and 0.08, respectively. The comparative results reveal that the object-and-SPDC approach achieves an increase of approximately 15 dB in the PSNR and an increase of approximately 11-fold in the SSIM compared with the object-only approach. From these results, we can conclude that our approach accurately reconstructs phase objects, achieving a phase resolution of 1.2 rad, consistent with the ground truth. This contrasts with the object-only method, which yields unresolved phase values.

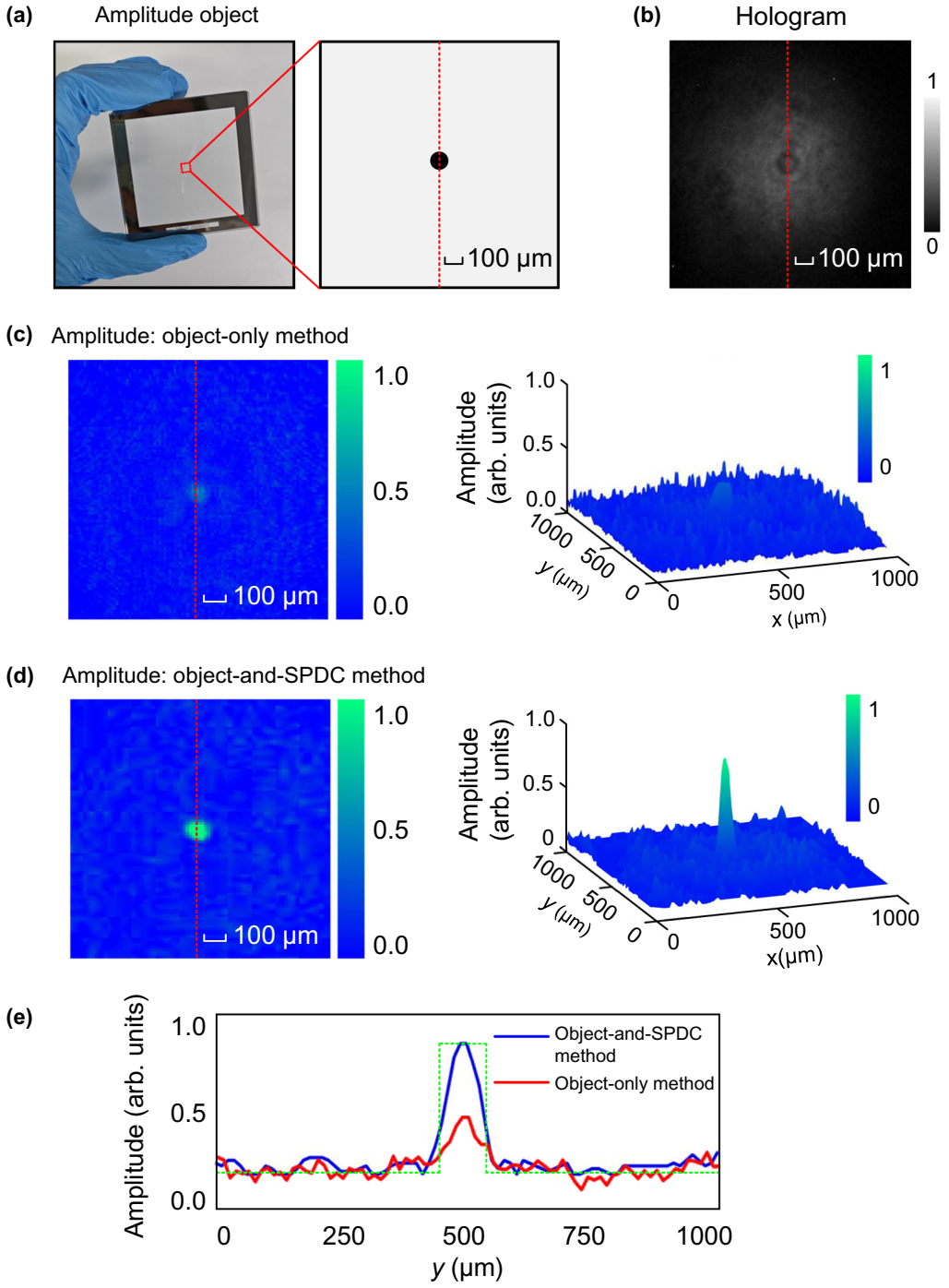


FIG. 4. Amplitude reconstruction. (a) Morphology of the amplitude object, which is a dot with a diameter of 100 μm. (b) Experimentally measured hologram of the amplitude object. (c) Amplitude reconstruction results obtained with the object-only method. The object-only method results in a blurry point with a small absorption peak, making it challenging to distinguish it from the surrounding noise. (d) Amplitude reconstruction results obtained with the object-and-SPDC method. The object-and-SPDC method reveals a bright green spot against a blue background, with a distinct absorption peak, accurately reconstructing the point's position with a diameter of 100 μm. Three-dimensional amplitude fluctuation shows a peak value of 0.8 for the object-and-SPDC method, while the object-only method achieves a peak value of just 0.4. (e) Cross sections of the reconstructions. The blue line, representing the object-and-SPDC method, shows an absorption peak of 0.8 and a peak width of approximately 100 μm, clearly depicting the dot's profile and closely matching the green line, which denotes the ground truth. The red line for the object-only method, with a peak absorption of 0.4, is less distinct and blends with the background noise.

The experimental procedure for an amplitude-only object, a dot with a diameter of 100 μm as shown in Fig. 4(a), follows a similar protocol. Initially, the hologram of the dot is captured within a limited area of 1000 × 1000 $\mu m^2$ to preserve its essential features, with the outcome shown in Fig. 4(b). Comparative results between the object-only method and our object-and-SPDC method are shown in Figs. 4(c) and 4(d). The size of the extrapolated hologram is 1200 × 1200 $\mu m^2$. The object-and-SPDC method produces a bright green spot against a blue background, with a significant absorption peak, accurately reconstructing the position of the point with a size of 100 μm. In contrast, the object-only method produces an unclear point with a small absorption peak, making it difficult to distinguish it from surrounding noise. The three-dimensional intensity distribution plot reveals that the peak value for the object-and-SPDC method is 0.8, while the peak value for the object-only method is only 0.4. To quantify the amplitude values experimentally, we examine the cross sections of the reconstructions in Fig. 4(e). The blue line represents the object-and-SPDC method and shows an absorption peak reaching 0.8 and a peak width of around 100 μm, revealing an obvious dot profile that almost matches the green line representing the ground truth. In contrast, the red line, representing the object-only method, shows an absorption peak reaching 0.4, which is difficult to distinguish from the background noise. The PSNR for the object-and-SPDC approach is 26.02 dB, while for the object-only approach it is 12.04 dB. The SSIM for the object-and-SPDC approach is 0.91, while for the object-only approach it is 0.14. The comparative results reveal that the object-and-SPDC approach achieves an increase of approximately 14 dB in the PSNR and an increase of 650% in the SSIM compared with the object-only approach. The analysis of these results underscores the efficacy of the object-and-SPDC method in facilitating detailed analysis of the dot's optical properties, demonstrating high SNR, high resolution, and recognition capabilities. Conversely,

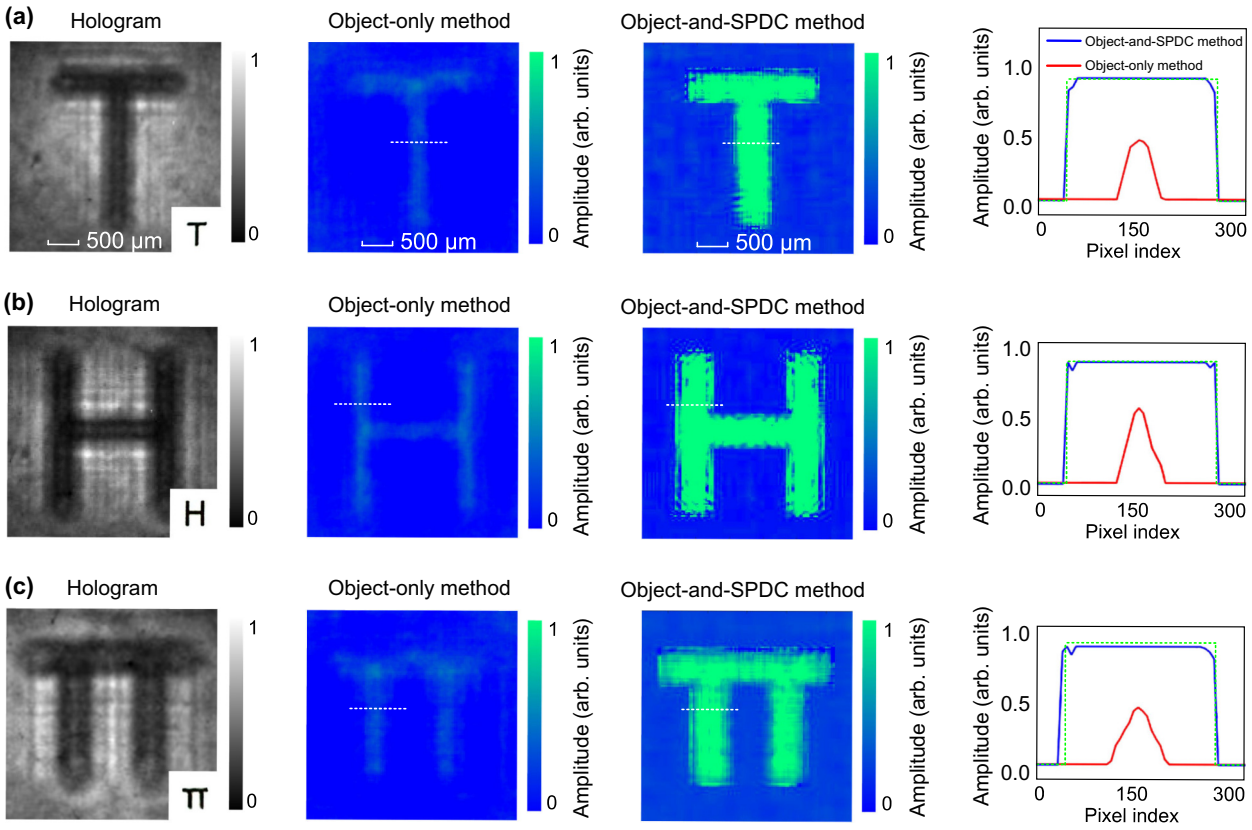


FIG. 5. Reconstruction results for characters. Hologram and the amplitude reconstruction results for characters (a) "T," (b) "H," and (c) "$\pi$." The first column presents the recorded holograms for each character. The second column shows the reconstructed amplitude results obtained with the object-only approach. The edges of the characters are hard to recognize. The reconstruction strength is notably weak, with a line width of only 200 μm, which significantly deviates from the ground truth. In contrast, the object-and SPDC approach, results for which are shown in the third column, provides clear edges and accurate structural features. The reconstructed line width of each character is 500 μm, which accurately reflects the original character's structure. The fourth column demonstrates the cross sections of the reconstructions along the dotted white line to compare the spatial resolution. The object-and-SPDC method demonstrates the accurate contour of the characters, while the object-only method provides a low-quality reconstruction.

the object-only method struggles with noise interference, limiting its ability to accurately reconstruct the dot's characteristics.

## IV. COMPLEX OBJECTS

Having validated the approach experimentally, we now move on to more complex objects. We initially use characters with a line width of 500 μm on a letter plate coated by a commercial company (Beijing Zhongke Shengze Technology Development Co., Ltd.), with details in Supplemental Material (see "Characters" in Supplemental Material [61]). The holograms and amplitude reconstruction results for the characters "T," "H," and "$\pi$" obtained with both object-only method and the object-and-SPDC method are shown in Fig. 5. The size of the hologram and the size of extrapolated hologram are $4000 \times 4000$ μm$^2$ and $4500 \times 4500$ μm$^2$, respectively. The first column showcases the holograms for each character, which capture the diffraction patterns generated by the interaction of photons with the respective characters. These patterns encode the essential information needed for accurate reconstruction. The second column presents the reconstructed amplitude results for the characters obtained with the object-only approach. The edges of the characters are difficult to recognize. The reconstruction strength is notably weak, with a line width of just 200 μm, showing a significant deviation from the ground truth. In contrast, the object-and-SPDC approach, as depicted in the third column, reveals detailed and high-fidelity reconstructions of the characters. The reconstructed line width of each character is 500 μm, faithfully reflecting the original structure of the characters. This method maintains clear edges and intricate features despite the presence of noise and limited initially captured data. The fourth column demonstrates the cross sections of the reconstructions along the dotted white line to compare the spatial resolution. The blue line, representing the object-and-SPDC method, demonstrates a clear contour of the characters, closely aligning with the green line, which represents the ground truth. In contrast, the red line, representing the object-only method, remains a low-quality reconstruction. The PSNR for the object-and-SPDC approach is 25.58 dB for "T," 25.76 dB for "H," and 25.39 dB for "$\pi$," while for the object-only approach it is 14.96 dB for "T," 15.85 dB for "H," and 15.56 dB for "$\pi$.'. The SSIM for the object-and-SPDC approach is 0.85 for "T," 0.89 for "H," and 0.83 for "$\pi$," while for the object-only approach it is 0.18 for "H," 0.19 for "T," and 0.22 for "$\pi$." The comparative results reveal that the object-and-SPDC approach achieves an increase of approximately 10 dB in the PSNR and an increase of approximately 450% in the SSIM compared with the object-only approach.

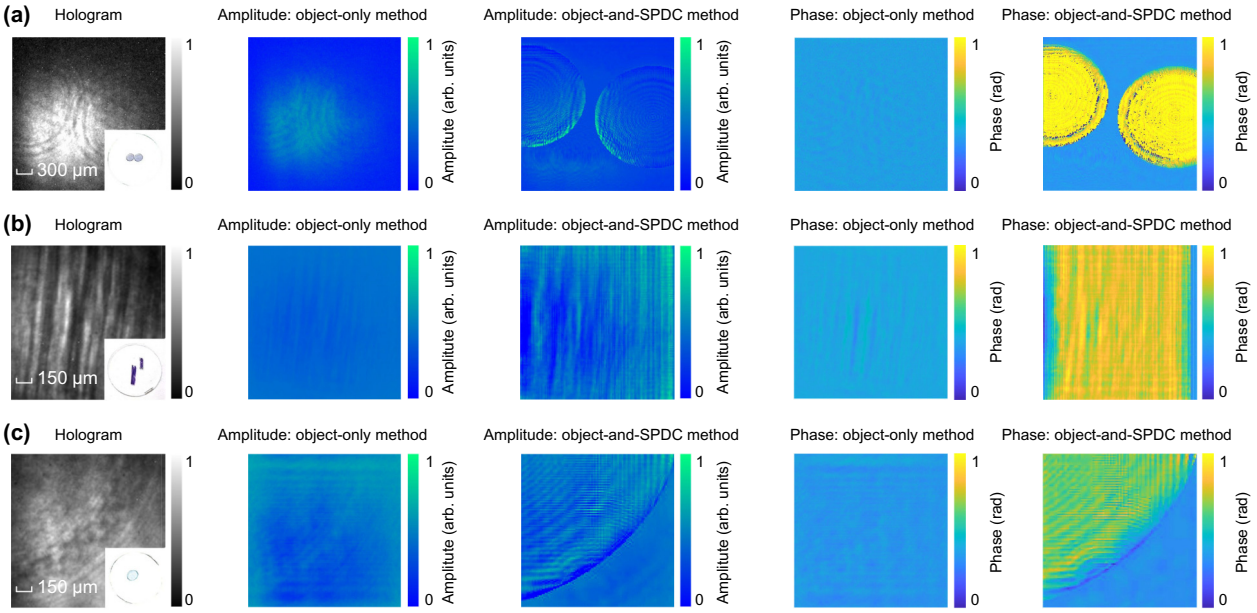


FIG. 6. Reconstruction results for biological specimens. Reconstructions of biological specimens obtained with the object-only method and the object-and SPDC method: (a) fertilized egg slices, (b) skeletal muscle, and (c) plant stems. The first column displays the recorded holograms, with insets showing the biological slides used in the experiment. With use of the object-and-SPDC method, the locations of the cells are clearly revealed in (a). The phase reconstruction distinctly outlines the edges of transparent cells, creating a strong contrast against the background. The linear features of muscle fibers are highlighted in (b), with amplitude and phase reconstructions both showing a uniform vertical distribution of thin fibers. The smooth edges of the plant stem cells are clearly delineated in (c). In contrast, the object-only method struggles to identify the locations, features, and edges of the cells, resulting in very weak amplitude reconstructions and blurred phase reconstructions, which limits its applicability in the biological field.

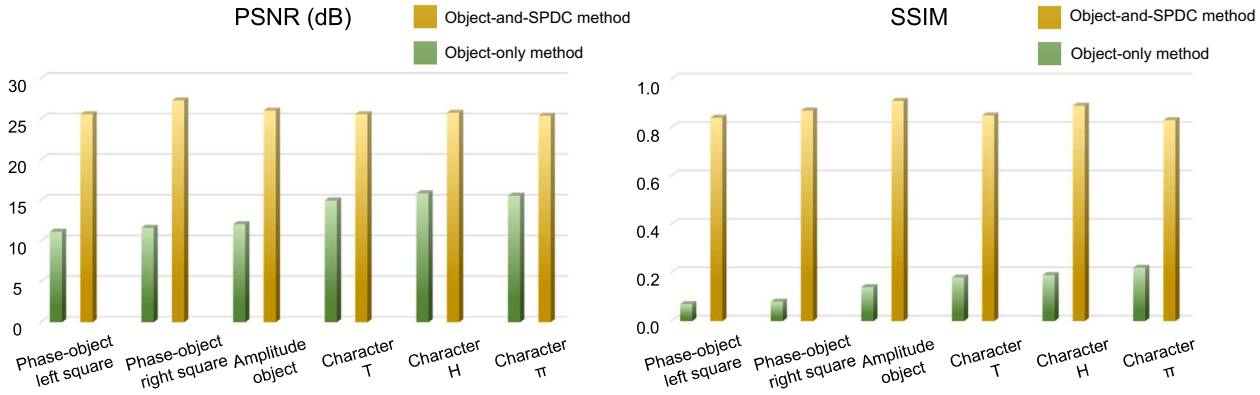


FIG. 7. Comparison of PSNR and SSIM in reconstruction. The comparative results reveal that the object-and-SPDC approach achieves an increase of up to 15 dB in the PSNR and an increase of approximately tenfold in the SSIM compared with the object-only approach.

We proceed to apply our approach to the holographic reconstruction of biological specimens, including fertilized egg slices, skeletal muscle, and plant stems, with the results shown in Fig. 6. These examples serve to demonstrate the practical applicability of our method to real-world samples with unknown and complex structures. The specimens are standard labeled biological slides sold by a biological research company, with enlarged details in Supplemental Material (see "Biological specimens" in Supplemental Material [61]). The phase variation of these biological samples is relatively small due to their limited optical thickness and low refractive index contrast. The first column in Fig. 6 showcases the recorded holograms, with the insets illustrating the biological slides used in the experiment. The size of the hologram for the fertilized egg slices is $2500 \times 2500\ \mu m^2$, while the extrapolated hologram measures $3000 \times 3000\ \mu m^2$. The size of the hologram for the skeletal muscle and plant stems is $1250 \times 1250\ \mu m^2$, while the extrapolated hologram measures $1500 \times 1500\ \mu m^2$. Figure 6(a) clearly reveals the location of the cells through the object-and-SPDC method. The phase reconstruction highlights the edges of transparent cells, providing a strong contrast against the background. The result indicates that high-frequency information provided by the object-uncorrelated photons increases edge sharpness. In Fig. 6(b), the linear features of muscle fibers are distinctly visible, with amplitude and phase reconstructions both depicting a uniform vertical distribution of thin fibers. Figure 6(c) clearly shows the smooth edges of plant stem cells, demonstrating the method's capability to preserve detailed structural information through effective hologram extrapolation and iterative reconstruction. These biological samples naturally exhibit nonuniform and continuous phase variations. The phase reconstructions clearly capture abrupt changes at the edges of structural features, demonstrating the method's sensitivity to phase gradients. This highlights the capability of the method to resolve both smooth and sharp phase transitions in more realistic and heterogeneous samples. In contrast, the object-only method yields very weak amplitude reconstructions and significantly blurred phase reconstructions, limiting its applicability in the biological field.

Overall, the object-and-SPDC method exhibits significant advantages over the object-only method in quantum holography. The object-and-SPDC method achieves recovery of the fine features by effectively integrating high-frequency information provided by the object-uncorrelated photons. Moreover, it boasts higher PSNR and SSIM values, indicating high-quality and noise-resistant imaging. The comparative results reveal that the object-and-SPDC approach achieves an increase of up to 15 dB in the PSNR and up to tenfold in the SSIM compared with the object-only approach. All numerical results for the different specimens are summarized in Fig. 7 and detailed in Supplemental Material (see "Evaluation results" in Supplemental Material [61]). Additionally, the object-and-SPDC method is better able to resist noise during imaging, ensuring that the imaging signal is not drowned out by noise but instead presents the features of the target object clearly. In contrast, the object-only method leads to image signals being submerged in noise, making them indistinguishable and yielding only artifacts or blurry images. In summary, the object-and-SPDC method demonstrates clear superiority in quantum holography, effectively improving imaging quality and reliability, and providing crucial technical support for the further advancement and application of quantum holography technology. This approach overcomes persistent challenges in current quantum holography, such as imperfect phase recovery, prolonged recovery time, and specific object requirements.

## V. DISCUSSION AND CONCLUSION

Quantum properties of light have catalyzed innovation in imaging techniques leveraging entanglement. This study

introduces a pioneering approach to quantum holography, harnessing spatial correlations and holographic algorithm. The findings are consistent with recent advancements in quantum holography research, highlighting the benefits of using photon pairs and exploiting the quantum properties of light for high-quality and noise-resistant imaging. Because the marginal spatial distributions of the signal and idler photon wave functions are identical, knowledge of one provides information about the other. This work builds upon these findings by introducing a method that extends the dimensions of the quantum holography channel, enabling the use of previously unrecorded hologram regions. The resolution of quantum holography is currently limited by the pixel size and the detection area. In practice, an additional ring of SPDC photons can be introduced around the full detection region to further increase resolution. This technique can be applied to existing detection areas to improve imaging performance even further. Experimental results indicate that the object-and-SPDC method has superior performance compared with conventional object-only methods, and can accurately reconstruct objects with high resolution and high SNR, while the object-only method struggles with noise and provides inaccurate amplitude and phase values. The object-and-SPDC method eliminates the need for a conventional $4f$ imaging system and directly records the diffraction fringes of the object. These findings underscore the potential of the object-and-SPDC method in quantum holography applications, where this method not only simplifies the optical setup but also extends the imaging field of view.

Besides, the ability to determine the photon distribution on the basis of the properties of the nonlinear crystal presents a significant advantage in quantum holography. By the leveraging of this capability, the process can be streamlined to require only the recording of the object-correlated photons, while object-uncorrelated photons beyond the detection area can be calculated. This eliminates the need to capture both object-correlated and object-uncorrelated photons, significantly reducing the recording time and detector size requirements, while maintaining accurate holographic reconstruction. This optimization is particularly advantageous for practical applications where efficiency and resource utilization are critical. Moreover, the decreased requirement of detector size contributes to the overall compactness and portability of the imaging system, enhancing its suitability for various environments and applications. Additionally, by minimization of data acquisition requirements, potential challenges related to data storage and processing can be mitigated. This allows more efficient utilization of computational resources and facilitates the integration of the quantum holography approach into existing imaging platforms and systems.

Future research directions may involve further optimization of the extrapolation propagation method, exploring applications in fast [65] and three-dimensional quantum reconstruction, and investigating potential integration with other quantum holography modalities such as quantum tomography and quantum sensing. Additionally, efforts could be directed toward increasing the robustness and scalability of the proposed quantum holography approach, particularly in complex imaging scenarios and nonlinear environments. Collaborative studies with experts from diverse fields such as material science, biophysics, and computational imaging could also offer valuable insights and foster interdisciplinary advancements in quantum holography. Furthermore, the development of novel quantum holography techniques tailored for specific applications, such as biomedical microscopy [66], holds promise for addressing pressing challenges and unlocking new opportunities in these domains. Overall, future research endeavors in quantum holography hold the potential to drive innovation and catalyze transformative advancements in imaging technology and quantum information processing.

## ACKNOWLEDGMENTS

This work was supported by the National Natural Science Foundation of China (Grants No. 62235009 and No. 92365107), the Innovation Program for Quantum Science and Technology (Grants No. 2021ZD0301400 and No. 2021ZD0301500), the National Key R&D Program of China (Grant No. 2019YFA0308700), the Program for Innovative Talents and Teams in Jiangsu (Grant No. JSSCTD202138), and the National Research Foundation of South Africa.

Each author contributed significantly to the work. Y.Y., Z.L., and Z.H. built the setup, performed the experiments, and contributed to data analysis. Y.Y., A.F., and Z.L. wrote the manuscript, with contributions from all authors. Y.Y., L.C., K.X., and Y.L. developed the concept. A.F., L.C., K.X., and Y.L. supervised the project.

The authors declare that they have no competing interests.

## DATA AVAILABILITY

The data that support the findings of this article are openly available [61].

## APPENDIX A: EXTRAPOLATION AND ITERATIVE RECONSTRUCTION ALGORITHM

In the extrapolation process, the recorded $M_0 \times N_0$ pixel hologram is initially extended to $M_1 \times N_1$ pixels, where $M_0 < M_1$ and $N_0 < N_1$ [67,68]. The amplitude of the extrapolated hologram is determined by the distribution of the SPDC photons, which can be calculated on the basis of the size and properties of the nonlinear crystal used in the generation of entangled photon pairs. The phase

of the extrapolated hologram is set to a constant or randomly distributed value. The quantity computed in the iterative routine is the extrapolated hologram. Then the iterative routine is used, where the photons propagate back and forth between the object plane and the recorded plane with two constraints, the support constraint and the absorption constraint [69,70]. The iterative routine is executed on the basis of the angular spectrum method (ASM) [71] to reconstruct the amplitude and phase of objects. "Forward propagation" refers to the propagation from the object to the detector, while "backward propagation'" refers to the reverse propagation from the detector to the object. The forward propagation of the wave field $U(x,y,0)$ at a distance $z_0$ is given by

$$U(x,y,z_0) = \mathcal{F}^{-1}\left\{\mathcal{F}[U(x,y,0)]\exp\left(-i2\pi z_0\sqrt{\frac{1}{\lambda^2}-f_x^{\,2}-f_y^{\,2}}\right)\right\}, \tag{A1}$$

and the backward propagation equation in the ASM is obtained by one taking the complex conjugate of the forward propagation equation:

$$U(x,y,0) = \mathcal{F}^{-1}\left\{\mathcal{F}[U(x,y,z_0)]\exp\left(i2\pi z_0\sqrt{\frac{1}{\lambda^2}-f_x^{\,2}-f_y^{\,2}}\right)\right\}, \tag{A2}$$

where $z_0$ is the propagation distance, $U(x,y,z_0)$ is the wave field on the recorded plane, and $U(x,y,0)$ is the wave field on the object plane.

Regarding the two constraints in the iterative process, the support constraint is applied first. As the object has a finite size, the distribution of the object $|\psi_O\rangle$ is confined with a mask in a finite space. Support constraint can extract the outline of the object, the space in the mask is set to 1, and the space outside the mask is set to 0. The implementation of the support constraint can increase the diffraction orders of the hologram, resulting in the extraction of more

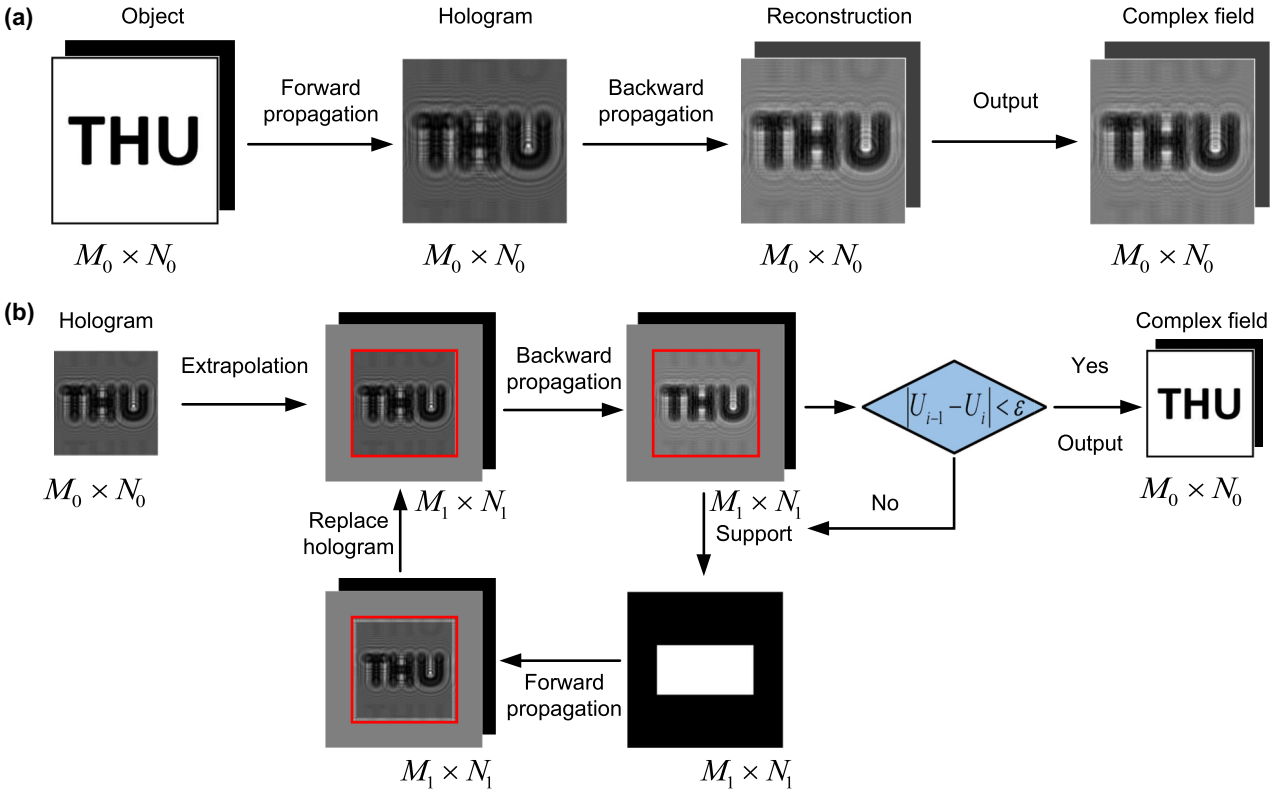


FIG. 8. Flow chart for the conventional object-only method and the proposed object-and-SPDC method. (a) Conventional object-only method for holographic reconstruction. The hologram is recorded through the forward propagation of the plane wave, and through backward propagation, the reconstructed complex field is obtained. (b) Proposed object-and-SPDC method for holographic reconstruction. After recording the hologram, we first extrapolate it with the object-uncorrelated photons. Iterations are then conducted with two constraints. When the reconstruction reaches the judging criterion $|U_{i-1} - U_i| < \epsilon$, the reconstructed complex field is output. Shown here for the characters "THU" as an example.

high-order fringes beyond the originally recorded hologram. Secondly, the absorption constraint is implemented. Since the number of signal photons cannot increase during scattering with the object, pixel values where the absorption is negative are set to zero. This constraint plays a crucial role in eliminating the twin image, significantly increasing the accuracy of the reconstructed object.

Figure 8(a) illustrates the conventional object-only method for holographic reconstruction. In this method, the hologram is recorded through the forward propagation of the plane wave, and through backward propagation, the reconstructed complex field is obtained. The overall object-and-SPDC method for holographic reconstruction is illustrated in Fig. 8(b). We divide the proposed method into six steps, and the reconstructed complex field is output after completion of these steps, shown here for the characters "THU" as an example:

(1) Initial hologram recording. Record the initial hologram of the object using the entangled photon pairs with a region of $M_0 \times N_0$ pixels. The probabilities obtained are directly proportional to the joint probability observed in a coincidence measurement between the photon pairs. Extend the hologram to $M_1 \times N_1$ pixels. The amplitude of the extrapolated pixels is determined by the distribution of the SPDC photons, and is updated after each iteration. The phase distribution is set to a constant value or randomly and is updated after each iteration.

(2) Backward propagation. Beam propagate back to the object plane following the principles outlined in Eq. (A2).

(3) Object plane operations. Apply the support constraint and absorption constraint on the reconstructed complex-valued object.

(4) Forward propagation. Beam propagate to the recorded plane following the principles outlined in Eq. (A1).

(5) Recorded plane operations. Replace the amplitude in the central $M_0 \times N_0$ pixels with the initially recorded hologram, while preserving the amplitude in the extended pixels. Keep the phase values unchanged. Restart the next iteration from step (2) until the judging criterion $|U_{i-1} - U_i| < \epsilon$ is reached.

(6) Quantum holographic reconstruction. After a number of iterations, output the complex value of the recorded plane in step (5). Reconstruct the object through Eq. (A2) to realize high-resolution and single-frame quantum holography.

## APPENDIX B: APPARATUS

The experimental setup for the heralded single-photon quantum holography is depicted in Fig. 2. Polarization-entangled photons are generated through the SPDC process on the basis of a Sagnac interferometer scheme [62–64]. A continuous-wave diode laser operating at 405 nm serves as the pump source. A 10-mm-long PPKTP crystal (Raicol Crystals) with a grating period of 10 μm is used for frequency-degenerate type-II quasi-phase-matched collinear SPDC. The crystal is antireflection coated at 405 and 810 nm. The temperature of the PPKTP crystal is maintained at 27.8 °C with stability of ±0.1 °C with the use of a temperature controller. The Sagnac interferometer comprises two flat mirrors and a dual-wavelength half-wave plate and a dual-wavelength polarizing beam splitter, both of which function effectively at the pump and output wavelengths. To eliminate the residual pump laser, 10 nm narrow bandwidth interference filters centered at a wavelength of 810 nm are used. A half-wave plate set at 45° is placed in the signal arm, and the output quantum state is set as $|\psi\rangle = (1/\sqrt{2})(|H\rangle\,|H\rangle - |V\rangle\,|V\rangle)$. The coincidence count of the photon pair is approximately 20 kHz.

The quantum holograms are captured with an ICCD (DH334T-18U-73, Andor) working at −30 °C, which enables the circumvention of the limitations imposed by point scanning, facilitating rapid and accurate capture of signal photons. The pixel size of the ICCD is 13 μm. Photons in the reference arm are coupled into a single-photon-counting module (SPCM). The output signal from the SPCM acts as the trigger for the ICCD to ensure single-photon imaging. To compensate for the delay introduced by the ICCD's triggering mechanism and the length of the optical single-mode fiber, an image-preserving delay line of 25 m is used, configured in a double-pass arrangement. The delay line comprises 12 lenses with a focal length of 500 mm and 14 mirrors in a double-pass configuration. The mechanical components are from LBTEK. The overall transmission efficiency of the optical path is about 30%. The ICCD operates in fast external mode with an optical gate width of 6 ns. The triggering mechanism of the ICCD introduces a 70 ns delay, while the overall optical length of the image-preserving delay line is 25 m, and the additional optical delay of the ICCD is adjusted to ensure the synchronicity of entangled photons. The triggered holograms are obtained through the accumulation of 200 images, each with an exposure time of 5 s. In our quantum holography scheme, noise levels are minimized as the ICCD camera is triggered only when a photon is detected in the object arm within a 5 ns window.

Although the SPCM is used to herald the arrival of idler photons, thereby discarding their spatial information during heralding, the spatial distribution is retrieved in a separate measurement. Specifically, we capture an image with the object removed, which effectively reflects the spatial distribution of the idler photons. Because of the correlated nature of the SPDC process, this distribution corresponds to the extrapolated region of the signal photon distribution. Ideally, simultaneous detection of both the signal photons and the idler photons with the use of two ICCDs would provide the most direct access to these spatial

correlations. However, under long exposure, the SPDC-generated spots are highly stable and consistently exhibit a uniform Gaussian-like distribution across acquisitions. Therefore, capturing the spatial profiles in two separate measurements is sufficient and does not affect the integrity of the spatial correlations used in the reconstruction.

To characterize the heralded single-photon source, the second-order correlation $g^2(\tau)$ for the signal field is measured, conditioned on successful detection of an idler photon count [72,73]. $g^2(0)$ represents the probability of detecting two photons in the signal arm simultaneously when the object photon is detected. In the experiment, $g^2(0)$ approaches 0 (see "Heralded single-photon source" in Supplemental Material [61]), indicating that the heralded single-photon source exhibits high quality, and the occurrence of two-photon or multiphoton events can be ignored.

## APPENDIX C: IMAGING SPACE

The entangled photon pair is generated through SPDC, leveraging the nonlinear optical properties of the crystal. In the realm of two-dimensional transverse wave vectors, the state of the photon pair is expressed as

$$|\psi_{SI}\rangle = \sum_{k=1}^{n} \frac{1}{n} |r_S\rangle_k \otimes |r_I\rangle_k , \tag{C1}$$

where $n$ is the total number of discrete transverse wave vector basis states $|r\rangle$ in the $x$ and $y$ components. The symbol $\otimes$ denotes the tensor product, indicating that the photon pairs are entangled in a joint quantum state. Each term $|r_S\rangle_k \otimes |r_I\rangle_k$ represents a pair of photons with correlated transverse wave vector components. Each basis $|r\rangle$ is derived by computation of the outer products of column vectors from the Hadamard transform matrix, expressed as $|r\rangle_k = |r\rangle_{(x,y)} = H_x \otimes H_y$. Photons are uniformly distributed across each orthogonal basis, forming a uniform light spot.

Considering that the generated signal and idler photons, following postselection in coincidences, form a high-dimensional single-photon state, with the spatial mode selected from a set of wave vector dimensions, the transfer of the generated signal and idler photons is then expressed as

$$|\psi_S\rangle = \sum_{k=1}^{n} \frac{1}{n} |r_S\rangle_k , \tag{C2}$$

$$|\psi_I\rangle = \sum_{k=1}^{n} \frac{1}{n} |r_I\rangle_k . \tag{C3}$$


[1] Y. Park, C. Depeursinge, and G. Popescu, Quantitative phase imaging in biomedicine, Nat. Photonics **12**, 578 (2018).

[2] G. Situ, Deep holography, Light: Adv. Manuf. **3**, 278 (2022).

[3] Y. Gao and L. Cao, Motion-resolved, reference-free holographic imaging via spatiotemporally regularized inversion, Optica **11**, 32 (2024).

[4] M. Deng, S. Li, A. Goy, I. Kang, and G. Barbastathis, Learning to synthesize: Robust phase retrieval at low photon counts, Light: Sci. Appl. **9**, 36 (2020).

[5] Z. Huang, P. Memmolo, P. Ferraro, and L. Cao, Dual-plane coupled phase retrieval for non-prior holographic imaging, PhotoniX **3**, 3 (2022).

[6] L. Shi, B. Li, C. Kim, P. Kellnhofer, and W. Matusik, Towards real-time photorealistic 3D holography with deep neural networks, Nature **591**, 234 (2021).

[7] Y. Peng, S. Choi, N. Padmanaban, and G. Wetzstein, Neural holography with camera-in-the-loop training, ACM Trans. Graph. (TOG) **39**, 1 (2020).

[8] D. Wu, J. Luo, G. Huang, Y. Feng, X. Feng, R. Zhang, Y. Shen, and Z. Li, Imaging biological tissue with high-throughput single-pixel compressive holography, Nat. Commun. **12**, 4712 (2021).

[9] M. Bernhardt, J.-D. Nicolas, M. Osterhoff, H. Mittelstädt, M. Reuss, B. Harke, A. Wittmeier, M. Sprung, S. Köster, and T. Salditt, Correlative microscopy approach for biology using X-ray holography, X-ray scanning diffraction and STED microscopy, Nat. Commun. **9**, 3641 (2018).

[10] M. Kagias, S. Lee, A. C. Friedman, T. Zheng, D. Veysset, A. Faraon, and J. R. Greer, Metasurface-enabled holographic lithography for impact-absorbing nanoarchitected sheets, Adv. Mater. **35**, 2209153 (2023).

[11] G. Xue, Q. Zhai, H. Lu, Q. Zhou, K. Ni, L. Lin, X. Wang, and X. Li, Polarized holographic lithography system for high-uniformity microscale patterning with periodic tunability, Microsyst. Nanoeng. **7**, 31 (2021).

[12] X. Lin, Y. Rivenson, N. T. Yardimci, M. Veli, Y. Luo, M. Jarrahi, and A. Ozcan, All-optical machine learning using diffractive deep neural networks, Science **361**, 1004 (2018).

[13] T. Zhou, X. Lin, J. Wu, Y. Chen, H. Xie, Y. Li, J. Fan, H. Wu, L. Fang, and Q. Dai, Large-scale neuromorphic optoelectronic computing with a reconfigurable diffractive processing unit, Nat. Photonics **15**, 367 (2021).

[14] E. Goi, S. Schoenhardt, and M. Gu, Direct retrieval of Zernike-based pupil functions using integrated diffractive deep neural networks, Nat. Commun. **13**, 7531 (2022).

[15] X. Fang, H. Ren, and M. Gu, Orbital angular momentum holography for high-security encryption, Nat. Photonics **14**, 102 (2020).

[16] K. T. Lim, H. Liu, Y. Liu, and J. K. Yang, Holographic colour prints for enhanced optical security by combined phase and amplitude control, Nat. Commun. **10**, 25 (2019).

[17] Y. Yang, A. Forbes, and L. Cao, A review of liquid crystal spatial light modulators: Devices and applications, Opto-Electron. Sci. **2**, 230026 (2023).

[18] Z. Huang and L. Cao, Quantitative phase imaging based on holography: Trends and new perspectives, Light: Sci. Appl. **13**, 145 (2024).

[19] J. Liu, I. Nape, Q. Wang, A. Vallés, J. Wang, and A. Forbes, Multidimensional entanglement transport through single-mode fiber, Sci. Adv. **6**, eaay0837 (2020).

[20] P.-A. Moreau, E. Toninelli, T. Gregory, and M. J. Padgett, Imaging with quantum states of light, Nat. Rev. Phys. **1**, 367 (2019).

[21] B. Courme, P. Cameron, D. Faccio, S. Gigan, and H. Defienne, Manipulation and certification of high-dimensional entanglement through a scattering medium, PRX Quantum **4**, 010308 (2023).

[22] J. Szuniewicz, S. Kurdziałek, S. Kundu, W. Zwolinski, R. Chrapkiewicz, M. Lahiri, and R. Lapkiewicz, Noise-resistant phase imaging with intensity correlation, Sci. Adv. **9**, eadh5396 (2023).

[23] X. Song, D. Xu, H.-B. Wang, J. Xiong, X. Zhang, D. Cao, and K. Wang, Experimental observation of one-dimensional quantum holographic imaging, Appl. Phys. Lett. **103**, 131111 (2013).

[24] A. F. Abouraddy, B. E. Saleh, A. V. Sergienko, and M. C. Teich, Quantum holography, Opt. Express **9**, 498 (2001).

[25] F. Devaux, A. Mosset, F. Bassignot, and E. Lantz, Quantum holography with biphotons of high Schmidt number, Phys. Rev. A **99**, 033854 (2019).

[26] T. Aidukas, P. C. Konda, A. R. Harvey, M. J. Padgett, and P.-A. Moreau, Phase and amplitude imaging with quantum correlations through Fourier ptychography, Sci. Rep. **9**, 10445 (2019).

[27] M. Gilaberte Basset, F. Setzpfandt, F. Steinlechner, E. Beckert, T. Pertsch, and M. Gräfe, Perspectives for applications of quantum imaging, Laser Photonics Rev. **13**, 1900097 (2019).

[28] Y. Yang and L. Cao, Quantum hyper-entangled system with multiple qubits based on spontaneous parametric down-conversion and birefringence effect, Opt. Quantum Electron. **56**, 12 (2024).

[29] R. Camphausen, Á. Cuevas, L. Duempelmann, R. A. Terborg, E. Wajs, S. Tisa, A. Ruggeri, I. Cusini, F. Steinlechner, and V. Pruneri, A quantum-enhanced wide-field phase imager, Sci. Adv. **7**, eabj2155 (2021).

[30] B. Sephton, I. Nape, C. Moodley, J. Francis, and A. Forbes, Revealing the embedded phase in single-pixel quantum ghost imaging, Optica **10**, 286 (2023).

[31] O. Wolley, T. Gregory, S. Beer, T. Higuchi, and M. Padgett, Quantum imaging with a photon counting camera, Sci. Rep. **12**, 8286 (2022).

[32] D. Abramović, N. Demoli, M. Stipčević, and H. Skenderović, Quantum holography with single-photon states, Phys. Rev. A **108**, 013709 (2023).

[33] T. Gregory, P.-A. Moreau, E. Toninelli, and M. J. Padgett, Imaging through noise with quantum illumination, Sci. Adv. **6**, eaay2652 (2020).

[34] H. Defienne, P. Cameron, B. Ndagano, A. Lyons, M. Reichert, J. Zhao, A. R. Harvey, E. Charbon, J. W. Fleischer, and D. Faccio, Pixel super-resolution with spatially entangled photons, Nat. Commun. **13**, 3566 (2022).

[35] R. Tenne, U. Rossman, B. Rephael, Y. Israel, A. Krupinski-Ptaszek, R. Lapkiewicz, Y. Silberberg, and D. Oron, Super-resolution enhancement by quantum image scanning microscopy, Nat. Photonics **13**, 116 (2019).

[36] D. Zia, N. Dehghan, A. D'Errico, F. Sciarrino, and E. Karimi, Interferometric imaging of amplitude and phase of spatial biphoton states, Nat. Photonics **17**, 1009 (2023).

[37] R. Chrapkiewicz, M. Jachura, K. Banaszek, and W. Wasilewski, Hologram of a single photon, Nat. Photonics **10**, 576 (2016).

[38] H. Defienne, B. Ndagano, A. Lyons, and D. Faccio, Polarization entanglement-enabled quantum holography, Nat. Phys. **17**, 591 (2021).

[39] S. Töpfer, M. Gilaberte Basset, J. Fuenzalida, F. Steinlechner, J. P. Torres, and M. Gräfe, Quantum holography with undetected light, Sci. Adv. **8**, eabl4301 (2022).

[40] G. B. Lemos, V. Borish, G. D. Cole, S. Ramelow, R. Lapkiewicz, and A. Zeilinger, Quantum imaging with undetected photons, Nature **512**, 409 (2014).

[41] G. Ortolano, A. Paniate, P. Boucher, C. Napoli, S. Soman, S. F. Pereira, I. Ruo-Berchera, and M. Genovese, Quantum enhanced non-interferometric quantitative phase imaging, Light: Sci. Appl. **12**, 171 (2023).

[42] J. Yang, R. Zhao, Z. Meng, J. Li, Q. Wu, L. Huang, and A. Zhang, Quantum metasurface holography, Photonics Res. **10**, 2607 (2022).

[43] Q. Wu, Z. Meng, J. Yang, and A. Zhang, Quantum process tomography on holographic metasurfaces, npj Quantum Inf. **8**, 46 (2022).

[44] C. Moodley and A. Forbes, Advances in quantum imaging with machine intelligence, Laser Photonics Rev. **18**, 2300939 (2024).

[45] L. Bian, H. Song, L. Peng, X. Chang, X. Yang, R. Horstmeyer, L. Ye, C. Zhu, T. Qin, D. Zheng *et al.*, High-resolution single-photon imaging with physics-informed deep learning, Nat. Commun. **14**, 5902 (2023).

[46] P. Cameron, B. Courme, C. Vernière, R. Pandya, D. Faccio, and H. Defienne, Adaptive optical imaging with entangled photons, Science **383**, 1142 (2024).

[47] H. Defienne, M. Reichert, and J. W. Fleischer, Adaptive quantum optics with spatially entangled photon pairs, Phys. Rev. Lett. **121**, 233601 (2018).

[48] T. Wheatley, D. Berry, H. Yonezawa, D. Nakane, H. Arao, D. Pope, T. Ralph, H. Wiseman, A. Furusawa, and E. Huntington, Adaptive optical phase estimation using time-symmetric quantum smoothing, Phys. Rev. Lett. **104**, 093601 (2010).

[49] L. Kong, Y. Sun, F. Zhang, J. Zhang, and X. Zhang, High-dimensional entanglement-enabled holography, Phys. Rev. Lett. **130**, 053602 (2023).

[50] H. Liang, H. Ahmed, W. Y. Tam, X. Chen, and J. Li, Continuous heralding control of vortex beams using quantum metasurface, Commun. Phys. **6**, 140 (2023).

[51] Y. Li, S. Huang, M. Wang, C. Tu, X. Wang, Y. Li, and H. Wang, Two-measurement tomography of high-dimensional orbital angular momentum entanglement, Phys. Rev. Lett. **130**, 050805 (2023).

[52] C. A. Casacio, L. S. Madsen, A. Terrasson, M. Waleed, K. Barnscheidt, B. Hage, M. A. Taylor, and W. P. Bowen, Quantum-enhanced nonlinear microscopy, Nature **594**, 201 (2021).

[53] Z. He, Y. Zhang, X. Tong, L. Li, and L. V. Wang, Quantum microscopy of cells at the Heisenberg limit, Nat. Commun. **14**, 2441 (2023).

[54] I. Kviatkovsky, H. M. Chrzanowski, E. G. Avery, H. Bartolomaeus, and S. Ramelow, Microscopy with undetected photons in the mid-infrared, Sci. Adv. **6**, eabd0264 (2020).
[55] D. Gabor, Holography, 1948–1971, Science **177**, 299 (1972).
[56] U. Schnars, C. Falldorf, J. Watson, W. Jüptner, U. Schnars, C. Falldorf, J. Watson, and W. Jüptner, *Digital Holography and Wavefront Sensing* (Springer, Hagen, Germany, 2015).
[57] R. Collier, *Optical Holography* (Elsevier, Murray Hill, New Jersey, US, 2013).
[58] https://github.com/THUHoloLab/Object-SPDC-quantum-holography.
[59] Y. Zhang, Z. He, X. Tong, D. C. Garrett, R. Cao, and L. V. Wang, Quantum imaging of biological organisms through spatial and polarization entanglement, Sci. Adv. **10**, eadk1495 (2024).
[60] H. Defienne, M. Reichert, and J. W. Fleischer, General model of photon-pair detection with an image sensor, Phys. Rev. Lett. **120**, 203604 (2018).
[61] See Supplemental Material at http://link.aps.org/supplemental/10.1103/b2hb-7zj5 for additional details and data analysis, including conceptual explanation, algorithm analysis, extrapolation validation, experimental details, and derivations of formulas. References [60,64,67–70,72,73] are also cited in Supplemental Material.
[62] Z. Li, D. Zhu, P. Lin, P. Huo, H. Xia, M. Liu, Y. Ruan, J. Tang, M. Cai, H. Wu *et al.*, High-dimensional entanglement generation based on a Pancharatnam–Berry phase metasurface, Photonics Res. **10**, 2702 (2022).
[63] T. Kim, M. Fiorentino, and F. N. Wong, Phase-stable source of polarization-entangled photons using a polarization Sagnac interferometer, Phys. Rev. A **73**, 012316 (2006).
[64] Z. Li, D. Zhu, J. Tang, M. Chen, Y. Ruan, J. Liu, H. Zhang, P. Chen, K. Xia, L. Zhang *et al.*, Quantum ghost imaging of a vector field, Opt. Express **32**, 5898 (2024).
[65] A. Mavian, Y. Xu, C. Li, and R. W. Boyd, Fast quantum ghost imaging with a single-photon-sensitive time-stamping camera, Opt. Lett. **50**, 594 (2025).
[66] L. Kong, J. Zhang, Z. Zhang, and X. Zhang, Quantum holographic microscopy, Laser Photonics Rev. **19**, 2401909 (2025).
[67] P. Gao and C. Yuan, Resolution enhancement of digital holographic microscopy via synthetic aperture: A review, Light: Adv. Manuf. **3**, 105 (2022).
[68] T. Latychevskaia and H.-W. Fink, Resolution enhancement in digital holography by self-extrapolation of holograms, Opt. Express **21**, 7726 (2013).
[69] T. Latychevskaia, Iterative phase retrieval for digital holography: Tutorial, JOSA A **36**, D31 (2019).
[70] C. Guo, C. Wei, J. Tan, K. Chen, S. Liu, Q. Wu, and Z. Liu, A review of iterative phase retrieval for measurement and encryption, Opt. Lasers Eng. **89**, 2 (2017).
[71] K. Matsushima and T. Shimobaba, Band-limited angular spectrum method for numerical simulation of free-space propagation in far and near fields, Opt. Express **17**, 19662 (2009).
[72] D. Höckel, L. Koch, and O. Benson, Direct measurement of heralded single-photon statistics from a parametric down-conversion source, Phys. Rev. A **83**, 013802 (2011).
[73] E. Bocquillon, C. Couteau, M. Razavi, R. Laflamme, and G. Weihs, Coherence measures for heralded single-photon sources, Phys. Rev. A **79**, 035801 (2009).